PAPER

Structurally-integrated resonators for broadband panel vibration suppression

IOP Publishing Smart Materials and Structures
Smart Mater. Struct. **29** (2020) 085010 (11pp) https://doi.org/10.1088/1361-665X/ab9148

Structurally-integrated resonators for broadband panel vibration suppression

Sih-Ling Yeh and Ryan L Harne

Department of Mechanical and Aerospace Engineering, The Ohio State University, Columbus, OH 43210, United States of America

E-mail: harne.3@osu.edu

Received 20 January 2020, revised 24 March 2020
Accepted for publication 7 May 2020
Published 29 June 2020

Abstract

There is limited understanding on interaction mechanisms that govern vibration attenuation when a small coverage of lightweight resonators are applied to practical engineering structures. To shed light on the unknowns, this research investigates lightweight elastomeric half cylindrical resonators attached to an aluminum panel using a small mass ratio around 3% and only around 1.7% coverage over the panel area. Finite element modeling of the system dynamics is complemented by corresponding experimental undertaking. The eigenfrequencies and eigenmodes of the resonators are scrutinized for the respective contributions provided towards broadband panel vibration suppression. The first order eigenmodes of the resonators are found to exert great influence on the starting mode for greater vibration attenuation, which may be tuned by the Young's modulus of the resonators. The concept of displacement polarization is established to probe how the resonator eigenmodes quantitatively contribute to attenuate the forced panel vibration. This study reveals how flexural panel vibration may be attenuated by transferring the vibration from the panel to resonators by virtue of modal interaction, and prepares a generalized analytical technique that may be used by other researchers studying multi-modal interactions between host structures and applied resonators. These findings may guide the future development of lightweight resonators with a small coverage area for vibration suppression in engineering applications.

Keywords: elastomeric resonator, broadband vibration attenuation, polarization analysis

Some figures may appear in colour only in the online journal

1. Introduction

Broadband vibration attenuation for structural panels has been of long-standing interest to researchers and industry. The concepts of constrained layer damping, bandgap, and tuned mass damper are commonly used in practices of vibration suppression. Constrained layer damping (CLD) laminates a flexible viscoelastic layer in between a stiff constraining layer and the underlying host structure layer. CLD dissipates vibration energy by the shear deformation in the viscoelastic layer according to the relative motion between the host and the constraining layer. Investigations on the stiffness of the constraining layer, the thicknesses of constraining and viscoelastic layers, the coverage area, and the loss factor of viscoelastic layer have illuminated the mechanisms of optimal design and implementation of CLD for many applications [1–4]. The studies find that optimized CLD layouts introduce only a small added weight [5, 6] while concurrently providing effective panel vibration dissipation [6]. The damping may be tailored by the shear modulus of the viscoelastic layer [7] as well as by the positions of CLD patches [4]. On the other hand, CLD methods of vibration control are often only effective in the mid to high frequency range, whereas many panel vibration concerns are concentrated in the lower frequency regime with wavelengths longer than the size of typical CLD solutions.

For bandgap-based methods of vibration suppression, destructive interference through Bragg scattered waves may be cultivated by periodic metamaterials. In a bandgap frequency regime, elastic waves are blocked, such as for silicone rubber stubs on an aluminum plate [8], rubber inclusions in an epoxy plate [9], double-sided pillars on a plate [10–12], and interconnected resonators attached to a plate [13]. The coupling

of the resonances in the metamaterials with wave propagation in the host structure may induce more than one bandgap. Yet, the bandgap frequency bandwidth may be limited, so that enhancement of the bandwidth necessitates more metamaterial mass, especially to suppress low frequency waves. For example, Yu *et al* [14] report an aluminum tube with periodic heavy metal copper rings coupled with rubber, shown to widen the flexural vibration bandgap. Sugino *et al* [15] present a method for bandgap estimation in one- and two-dimensional locally resonant metastructures. With a sufficient number of resonators, the normalized bandgap width is found to be $\sqrt{1+\mu}-1$ [15], where μ is the mass ratio between the added resonators and host structure. The findings clearly quantify the significance of the mass ratio on the bandgap frequency bandwidth. In addition, inducing a bandgap often requires a sufficiently large number of periodic structures while increasing the number of added resonators also enhances the wave attenuation efficiency [16, 17]. Based on the attenuation mechanism in bandgaps, the waves are required to pass through the designed periodic metamaterials to be blocked [18]. This also suggests that the protected environment may need to be surrounded by periodic metamaterials to prevent waves from propagating in the environment [19], which could be a limitation in engineering applications.

The classic tuned mass damper (TMD) is a mass interfaced with the host structure through a parallel spring and damper. By designing the resonant frequency of the TMD to be near to the host structure resonance, host structure vibration is suppressed. Yet, the phenomenon occurs in a relatively narrow frequency range by way of transferring energy from the host structure to the TMD. Researchers have investigated numerous methods to overcome this fundamental limitation of TMD-based vibration control. The application of multiple TMDs with tuning variations is one way to enhance the effectiveness and robustness of vibration suppression by the resonant phenomenon. Studies find that optimized multiple TMDs deliver greater vibration attenuation than the optimized single TMD even if the multiple TMDs in total constitute the same added mass ratio as the single TMD [20–23]. Furthermore, Li and Ni [24] find that non-uniformly distributed TMDs are more effective than uniformly distributed TMDs. Igusa and Xu [20] indicate that the width of the frequency range is proportional to the square of the mass ratio.

Extending from a single mode to multiple modes for broadband vibration control, Zuo and Nayfeh [25] and Jacquot [26] discuss how damping characteristics of multiple TMDs influence the effectiveness of vibration attenuation. Employing arrays of TMDs may lead to large mass ratios or large coverage areas when compared to the host panel mass and surface area. For instance, Yu and Lesieutre [27] develop metamaterial vibration absorbers embedded in a sandwich panel that substantially suppress panel vibration of the two lowest order modes yet require a mass ratio of nearly 30%. Nouh *et al* [28] propose a host aluminum plate with cavities filled with viscoelastic membranes that support periodic small aluminum masses. Although this embodiment is also effective for broadband vibration control [28], the coverage area is 60% of the plate, while the added mass is 39% of the host structure. To reduce the metamaterial weight, Sun *et al* [29] develop periodic plastic frames filled with rubber membranes that support iron discs to attenuate steel panel vibration in the low frequency regime. Although the mass ratio of the solution was only 6% [29], the area over which the metamaterial covered the plate was around 50%. In summary, these studies reveal that broadband panel vibration suppression by a small application of lightweight resonators is a challenging technical target that remains to be achieved.

Recently, the authors investigated the use of lightweight metamaterial cylindrical inclusions embedded in a tube for transverse vibration dissipation of the tubular structure [30]. Optimization efforts revealed the mechanisms of broadband vibration attenuation exerted by the metamaterials on the host tubular structure, showing frequency sensitive TMD and CLD responses from the same metamaterial embodiments [31]. Given the success of such cylindrical metamaterials to control broadband and low frequency vibration of tubular structures, this research searches for strategies by which to translate such capability to broadband vibration attenuation for panels. Here, to make the cylindrical geometry compatible for application to a flat panel host structure, the design of the lightweight resonator is a half cylinder with flat surface that is attached to the host panel.

Building from this preliminary concept, this report investigates the application of lightweight half cylindrical resonators to a thin panel to attenuate flexural vibration and explores the mechanisms by which such resonators deliver broadband attenuation of host panel vibration. Following this introduction, the resonator specimen design, experimental undertakings, and finite element modeling are described as foundation on which to undertake subsequent technical investigations. Using these resources, the influences of the resonator Young's modulus and geometry on vibration attenuation mechanisms are studied in detail revealing significant coupling of multimodal vibrations in the resonator with host structural response. The discoveries stemming from this resource are summarized in a concluding section.

2. Specimen descriptions and investigation methods

This section first describes the panel and resonator specimens considered throughout this research. Next, the experimental methods are introduced along with the composition of the finite element model. Finally, the finite element model is validated against experimental data to prepare for the detailed investigations in section 3.

2.1. Resonator description

The elastomeric resonator and geometric features of the resonator design are presented in figure 1(a). The resonator is a half cylinder of outer radius R^h and length L. The cross-section geometry of the resonator has three parts, including an outer half circular annular layer of thickness t, radially arrayed beams, and a semicircle core of radius R^c, as shown in figure 1(a). The

open angle ratio α/β is the ratio between the angle inscribed by the void and the angle of the periodic radially arrayed beam in the middle layer. The geometric parameters of the half cylindrical resonator are listed in table 1. This study considers resonators fabricated using one of three durometers of silicone rubber (Smooth-On, Inc.). The silicone rubbers include Ecoflex 00–10 (EF10, Shore hardness 00–10), Mold Star 15 S (MS15, Shore hardness 15 A), and Mold Star 30 (MS30, Shore hardness 30 A).

Table 1. Geometric parameters of the panel and half cylindrical resonator.

item	unit	value
panel length, a	mm	304.8
panel thickness, h	mm	1.6
resonator length, L	mm	20
resonator outer radius, R^h	mm	10
resonator annular thickness, t	mm	1.5

2.2. Host structure and experimental setup

In this study, the host structure is a freely suspended, square aluminum panel of length a and thickness h. The geometric parameters of the panel are in table 1. By way of the mode shapes with peak displacements at the edges and corners, here the half cylindrical resonators are attached on the square aluminum panel at the bottom panel edge with respect to the suspension, as shown in figure 1(b). The bond between panel and half cylindrical resonators is made by silicone sealant, to be compatible with the bulk material of the resonators. The positions of the resonators are labeled as 1, 2, 3, and 4 in figure 1(b). Depending on the cross-section geometry, the mass of a resonator examined here varies from 2.4 g to 3.4 g. This corresponds to a total mass ratio between the four resonators and host panel from 2.4% to 3.3%. The coverage area of the four resonators is only over 1.7% of the aluminum panel surface.

This study employs roving accelerometer modal hammer impact evaluations to determine the frequency response of the panel. For each measurement, the modal hammer (PCB 086C01) delivers an impact at a position represented by the green triangle marker in figure 1(b). In order to determine the global acceleration of the panel, the 25 measurement positions represented by the red circle markers in figure 1(b) are distributed periodically on the panel. The accelerometer (PCB 352A24) is mounted to the rear of the panel with respect to the impact direction. Each experiment involves the measurements of the 25 positions to generate the transfer function (TF) between output global acceleration and the input force providing by the modal hammer. The output global acceleration is computed from the square root of sum of squares of the acceleration Fourier transform at each location, while the input force amplitude is sought for each corresponding measurement. The experimental global TF is an average of the individual TFs from the 25 positions. By extracting the imaginary part of the TF for each position at the experimentally determined natural frequencies, the experimental mode shapes of the bare panel are reconstructed [32]. The panel experimental mode shapes for the eight lowest order modes are shown in figure 2(a).

2.3. Finite element model formulation and validation

The frequency response of vibration for the panel is investigated via finite element (FE) modeling to parallel and support the experimental efforts. An FE model (COMSOL Multiphysics, Stockholm, Sweden) is created using shell elements for the panel [33] and solid elements for the resonators. The boundaries and parameters in any given experiment are likewise used in the FE model, as shown in figure 1(c). The material properties of the aluminum panel are provided in table 2.

The natural frequencies and mode shapes of the bare panel determined by the FE model are shown in figure 2(b). Considering the simulated natural frequencies of the bare panel, the absolute deviations with respect to experimental data for the ten lowest order modes are less than 6%. For the mode shapes, clear agreement is observed comparing FE predictions and experimental results for the bare panel in figure 2. The results suggest that the modal hammer technique employed in experiments sufficiently excites the ten lowest order modes, and the suspension technique sufficiently reproduces free boundary conditions of the panel.

After validating the efficacy of the FE model approach, the following sections of this report detail simulations of TF frequency response between global panel acceleration and input force with and without the half cylindrical resonators. The material properties of the half cylindrical elastomeric resonators are listed in table 2. The interfacial surfaces between the panel and the resonators are assumed to maintain perfect contact. The FE vibration responses investigate through calculating the surface integration of the panel acceleration over the panel surface area divided by the input forced amplitude to generate the TF between global acceleration and force. Linear responses are examined for sake of the small absolute values of displacement considered for the panel with resonators.

The objective of this study is to uncover vibration attenuation mechanisms of structurally-integrated resonators on a host, vibrating panel. The spectral and modal responses of resonators and the panel are explored through the subsequent experimental studies and FE simulations that probe origins of vibration energy transfer and attenuation.

3. Results and discussions

To understand the coupling between the panel and resonators that govern vibration attenuation mechanisms, this section leverages complementary FE and experimental efforts to probe the origins of the system dynamics and interactions. In each section following, the TF frequency responses of the panel with and without the resonators are considered, using resonators classified by labels such as A, G, and so on. These labels indicate material or geometric changes of the resonators, which are respectively described in the section text.

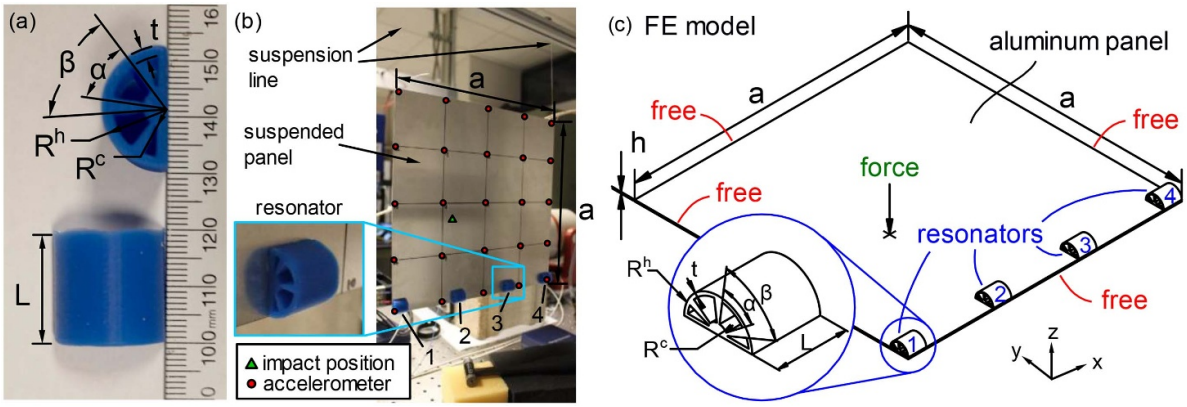

Figure 1. (a) Geometric notations of the half cylindrical resonators. (b) Experimental setup of modal hammer impact tests. (c) Finite element (FE) model of the panel with half cylindrical resonators.

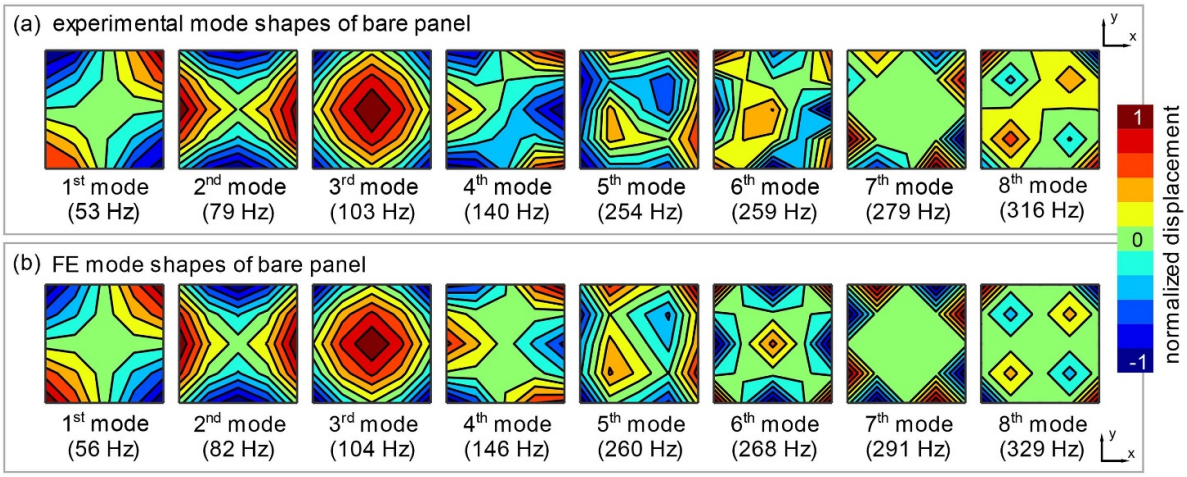

Figure 2. (a) Experimental and (b) finite element (FE) mode shapes of bare panel for eight lowest order modes.

3.1. Change of resonator Young's modulus governs vibration attenuation mechanism

The experimental and FE TF frequency responses of the panel without and with resonators A, B, and C are respectively presented in figures 3(a) and (b). The resonators A, B, and C are fabricated using silicone rubbers, EF10, MS15, and MS30 in increasing bulk modulus. In the insets, grey color refers to EF10, cyan color refers to MS15, and blue color refers to MS30. The cross-sectional geometry of resonators A, B, and C are identical so that the core radius ratio and open angle ratio of the three resonators are 0.3 and 0.75, respectively. At around 140 Hz, the experimental and FE TF peak attenuation between the response of bare panel and panel with resonator A are 7.65 dB and 8.94 dB, respectively. Both experiment and FE simulation indicate that frequencies around 140 Hz and greater are attenuated by resonator A. For resonators B and C, the TF peak attenuation are around 8 dB in the experiment and 22 dB in FE simulation. Except for the experimental TF response at around 275 Hz, the greater effectiveness of vibration attenuation for resonators B and C is evident at frequencies 255 Hz and up. Overall, the FE results agree well with experiments.

Table 2. Material properties of the panel and half cylindrical resonators.

	aluminum panel	EF10	MS15	MS30
Young's modulus, kPa	70×10^6	200	600	800
Poisson's ratio	0.33	0.49	0.49	0.49
density, $kg\ m^{-3}$	2700	1145	1145	1145
structural loss factor	0.001	0.2	0.2	0.2

The total displacement contours for the five lowest order eigenmodes for resonator A are shown in figure 3(c). These modal characteristics are determined from FE based modal analyses solely of the half cylindrical resonators with bottom surfaces fixed. The displacements are greatly exaggerated in figure 3(c) for ease of visualization. The total displacement is the square root of the sum of square of displacement component in the x-, y-, and z-directions. Figure 3(d) exemplifies that the Young's modulus of the resonators has a significant influence on the resonator eigenfrequencies, although the scaling is mostly uniform in this frequency range. With

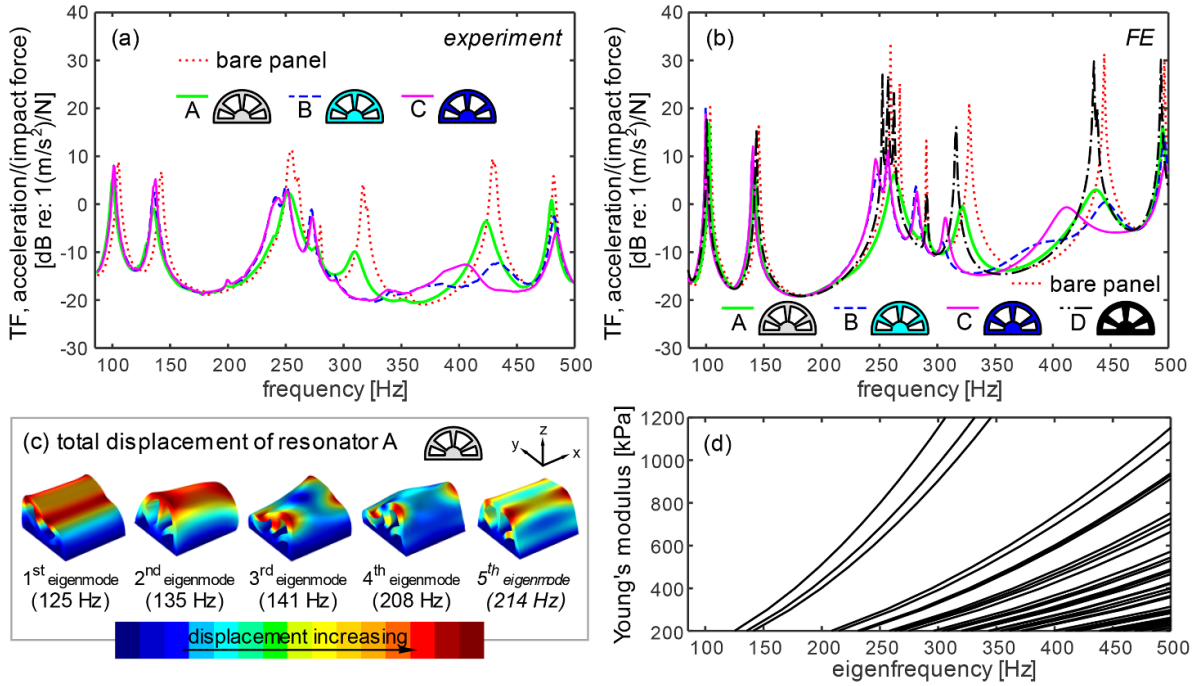

Figure 3. (a) Experimental and (b) finite element (FE) frequency responses of the panel with several sets of resonators with different Young's moduli. (c) FE mode shapes for the five lowest order eigenmodes of resonator A. (d) FE predictions of resonator eigenfrequency as function of Young's modulus.

identical cross-sectional geometry of resonators, the eigenfrequency of resonator increases by a factor of the square root of the Young's modulus, which agrees with prior findings [31].

Here, the term 'starting mode' is used to identify the modal region of the resonator around which the more substantial vibration attenuation is achieved, for which greater frequencies of the panel vibration TF are more highly suppressed. A comparison between the panel TF in figure 3(b) and the eigenfrequencies of the resonator eigenmodes in figure 3(d) helps to identify that the 'starting mode' for resonators A, B, and C is the first resonator mode. The resonator A shows more prominent panel vibration suppression at frequencies around 150 Hz in figures 3(a) and (b) because the first eigenmode in figure 3(d) occurs around 125 Hz. Likewise, figure 3(d) indicates that resonators B and C have the first eigenmodes around 217 Hz and 250 Hz, respectively. Considering figures 3(a) and (b), for frequencies greater than these eigenfrequencies, the panel TF frequency responses are suppressed when using resonators B or C. Such trend also agrees with prior observations of elastomeric inclusions in poroelastic media for sake of promoting vibration [31] and sound attenuation [34].

To clarify the relations between the first resonator eigenmode and 'starting mode' in the panel frequency response where the resonators exhibit greater vibration suppression, the stiff resonator D is considered with Young's modulus of 70 GPa, having the same cross-sectional geometry as resonators A, B, and C. By having a modulus several orders of magnitude greater than the other silicone rubber resonators A, B, and C and by having the same modulus as the panel, the resonator D simulates a static mass added to the panel equivalent to the silicone rubber resonator mass. In figure 3(b), the black dot-dash curve shows the FE TF frequency response of panel with resonator D. Figure 3(b) shows that the effect of the resonator D application to the panel is minor mass loading to resonances, shifting the forced resonances downward slightly in frequency and amplitude. Because the first eigenmode of resonator D is around 74 kHz, there is no more prominent panel vibration attenuation provided in the 85 Hz to 500 Hz frequency range of the panel. These findings confirm that the resonator *dynamic mass* and *dynamic stiffness* together yield the enhanced vibration suppression rather than static mass and stiffness.

3.2. *Tailoring open angle and core radius ratios to govern resonator dynamic stiffness and mass*

Figures 4(a) and (b) present the experimental and FE TF frequency responses of the bare panel and panel with resonators A, E, and F. Here, the open angle ratios α/β of resonators A, E, and F are 0.75, 0.58, and 0.42, respectively. The bulk material constituting the resonators is EF10, while the core radius ratio R^c/R^h of A, E, and F is 0.3. In figures 4(a) and (b), the greater reductions in the panel with resonators A, E, and F are observed in both experiment and FE simulation at frequencies 140 Hz and greater. Based on the attenuation mechanism of 'starting mode' introduced in section 3.1 and resonator eigenfrequencies as a function of open angle ratio in figure 4(c), it is seen that the 'starting mode' occurs at around 140 Hz since the first eigenmodes of resonators A, E, and F are at 125 Hz, 142 Hz, and 149 Hz, respectively. Considering the peak attenuations, both experimental and FE frequency responses at around 250 Hz and 325 Hz show the dramatic attenuations when decreasing the open angle ratio from 0.75

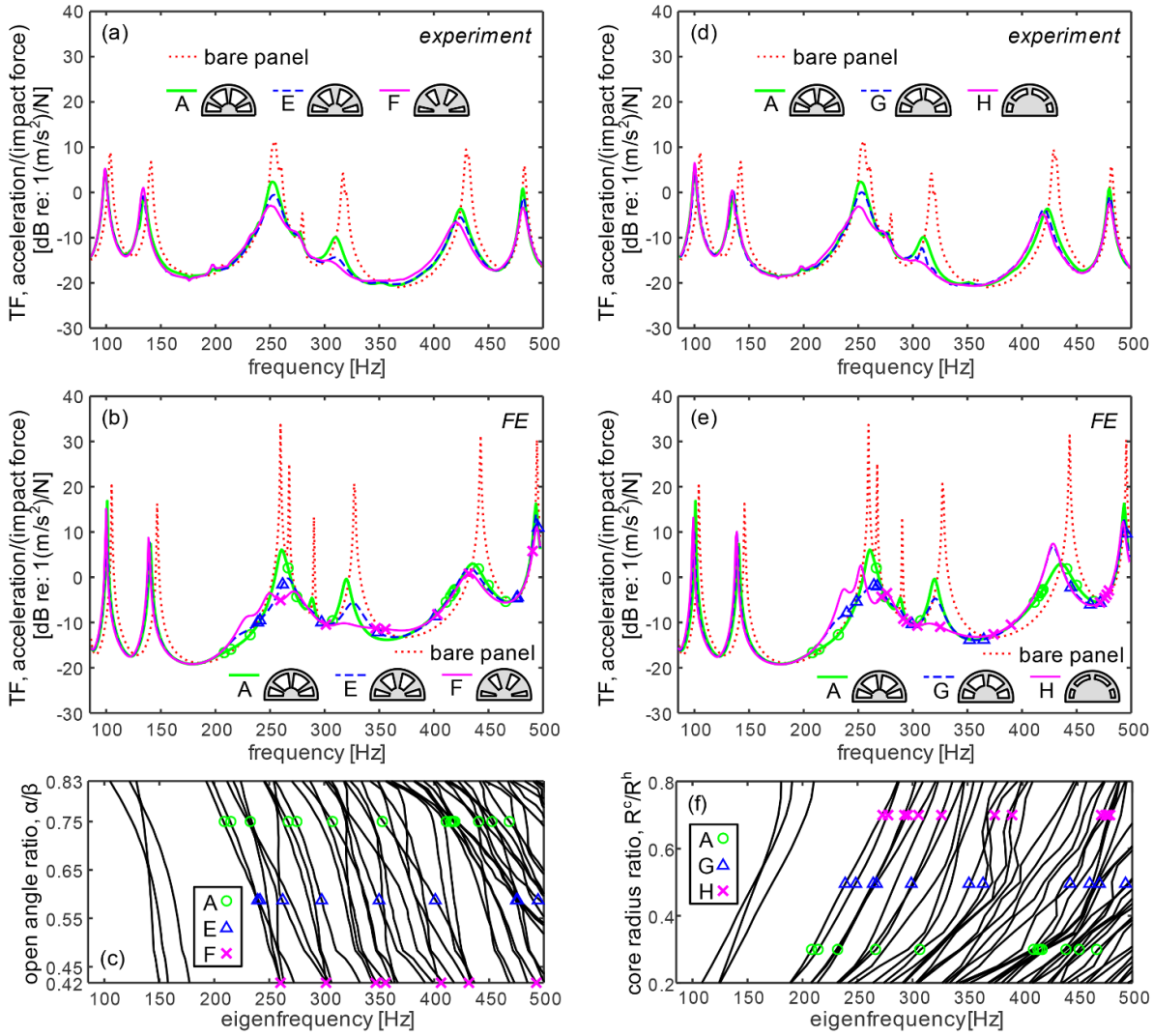

Figure 4. (a) Experimental and (b) FE frequency responses of the panel with three sets of resonators with open angle ratios α/β of A: 0.75, E: 0.58, and F: 0.42. (c) FE model predictions of resonator eigenfrequency as function of open angle ratio. (d) Experimental and (e) FE frequency responses of the panel with three sets of resonators with core radius ratios R^c/R^h of A: 0.3, G: 0.5, and H: 0.7. (f) FE model predictions of resonator eigenfrequency as function of core radius ratio.

Table 3. Ratio of polarization (ROP) values of displacement components in the x-, y-, and z-direction in resonator A for the six lowest order eigenmodes.

eigenfrequency (Hz)	125	135	141	208	214	231
ROP_x (%)	0	89	19	6	4	4
ROP_y (%)	91	1	63	36	14	46
ROP_z (%)	9	10	18	58	82	50

(resonator A) to 0.42 (resonator F). Overall, the FE results are in good agreement with experimental trends, encouraging attention to the specific mechanisms of the vibration attenuation induced by the resonators.

As seen in figure 3(c), the eigenfrequency of the resonator slightly decreases for increase in the open angle ratio α/β. For an increase in the open angle ratio α/β, the radially arrayed beams in the middle layer become less massive and become more slender. Based on the trends of decreasing eigenfrequency by increasing the open angle ratio, it reveals the influential aspect of tuning the open angle ratio of the resonators is to reduce the dynamic stiffness of the middle layer and further lead to a decrease of the eigenfrequency.

Figures 4(d) amd (e) present the experimental and FE TF frequency responses of the bare panel and panel with resonators A, G, and H. The core radius ratios R^c/R^h of resonators A, G, and H are 0.3, 0.5, and 0.7, respectively. The open angle ratio α/β of resonators A, G, and H is 0.75, while these resonators are fabricated using the bulk material EF10. As observed in figures 4(d) and (e), the vibration attenuation from the introduction of the resonators uniformly occurs around the panel mode near 140 Hz. By studying the resonator eigenfrequencies in figure 4(f) as a function of core radius ratio, this suggests that the greater attenuation of panel vibration provided by the lightweight resonators corresponds to activation of modes starting around the first eigenmode of the resonators. Similar

to the trends of the change of open angle ratio, when increasing the core radius ratio from 0.3 (resonator A) to 0.7 (resonator H), the more dramatic attenuations occurs at around 250 Hz and 325 Hz in both experimental and FE results in figures 4(d) and (e). The modal dependence of vibration attenuation induced by core radius ratio will be fully assessed in section 3.3.

The relationship between change of the core radius ratio R^c/R^h and the eigenfrequency of resonator is shown in figure 4(f). Generally, the resonator eigenfrequencies increase for increase in the core radius ratio R^c/R^h. For an increase in the core radius ratio, the radially arrayed beams in the middle layer become shorter, and the core becomes more massive. Based on the trends of increasing eigenfrequency by increasing the core radius ratio, the results suggest that the radius ratio of the resonators also contributes to change the resonator dynamic stiffness.

3.3. Polarized resonator eigenmodes for vibration attenuation

The eigenmodes of the resonators do not equally engage with the forced panel modes, as evident by the distinct frequency ranges where each resonator is better suited for broadband vibration suppression. To explore how the resonator eigenmodes suppress flexural vibration, the polarization of displacements in the x-, y-, and z-directions of the resonators is quantified. The ratio of polarization ROP_p [35, 36] in the p direction for the volume V of a resonator eigenmode is

$$ROP_p = \frac{\int\limits_V (u_p)^2 dV}{\int\limits_V \left[(u_x)^2 + (u_y)^2 + (u_z)^2\right] dV} \tag{1}$$

Here, u_x, u_y, and u_z are respectively the displacement components in the x-, y-, and z-directions of the resonator. The subscript p is respectively replaced by x, y, and z to compute the ratios of polarization in the corresponding directions. The volume integration of the sum of squares of displacement components in the x, y, and z-directions is employed to understand the dynamic response of the resonators. The ratios of polarization for the six lowest order eigenmodes of resonator A are presented in table 3 using the FE simulation results. The dominant displacement components of the first eigenmode at 125 Hz, the second eigenmode at 135 Hz, and the third eigenmode at 141 Hz are respectively concentrated in the y-, x-, and y-directions. Because the panel vibration is mostly flexural or transverse to the $x-y$ plane, such resonator eigenmodes do not greatly contribute to suppress panel motion. On the other hand, table 3 indicates that the fourth resonator eigenmode at 208 Hz, the fifth eigenmode at 214 Hz, and the sixth eigenmode at 231 Hz for resonator A are polarized mostly in the z-axis.

In figure 4(b), the eigenmodes with $ROP_z > 0.5$ of resonators A, E, and F are respectively marked as the green circle, blue triangle, and magenta cross markers. Considering the resonator eigenmodes having $ROP_z > 0.5$ at around 250 Hz and 325 Hz in figure 4(c), the orders of the resonator F eigenmodes are less than resonator A. The lower order resonator eigenmodes may be easier to excite, which is beneficial to increase vibration attenuation behavior when compared to the higher order eigenmodes, which require more energy to activate [34]. This helps to explain why resonator F provides greater panel vibration attenuation observed in figures 4(a) and (b) at 250 Hz and 325 Hz than resonator A. On the other hand, as seen in figures 4(a) and (b), the vibration attenuation at frequencies greater than 400 Hz is less influenced by the change of open angle ratio because the order of resonator eigenmodes in such frequency range are greater and have less energy for vibration suppression. The green circle, blue triangle, and magenta cross markers in figure 4(e) refer to the eigenmodes with $ROP_z > 0.5$ of resonators A, G, and H, respectively. The fact that the lower order resonator eigenmode may have greater energy for vibration attenuation illuminates the more dramatic vibration attenuations delivered by resonator H at 250 Hz and 325 Hz in figures 4(d) and (e). These findings indicate the lower order resonator eigenmodes with greater polarized displacements in the z-axis have more influences on the substantial transverse vibration attenuations.

3.4. Relating resonant modes to panel vibration suppression

The forced panel vibration distributions for the third, fourth, fifth, and sixth modes are presented in figure 5. From left to right, figures 5(a)–(d) respectively show results for the bare panel, panel with resonator A, panel with resonator B, and panel with resonator C. The total displacement of the system is shown on a normalized contour scale of total displacement per each respective sub-plot. For the third and fourth resonant panel modes with resonators A, B, or C in figures 5(b)–(d), the greatest deformations are localized in the two resonators at the corners of the panel. Except for the fourth mode with resonator A having approximate 8 dB of peak TF attenuation, these are not modes that show substantial reduction of panel vibration in figures 3(a) and (b). On the other hand, the fifth and sixth modes of the panel with resonators A, B, and C respectively shown in figures 5(b)–(d), reveal greatest deformation in the resonators, while the panel vibrations are minimized. To uncover an explanation for such vibration attenuation, it is necessary to study the relationships between the eigenmodes of the resonators and the corresponding forced displacement distributions of the resonators on the panel.

The total displacement profiles of resonators A1, A2, A3, and A4 at the fourth mode around 139 Hz are presented in figure 5(e). The resonators A1, A2, A3, and A4 refer to the resonator A samples located at positions 1, 2, 3, and 4 on the panel, as shown in figure 1(c), respectively. For the four resonators, the greatest deformations are localized in specific regions along the top of the annular layer. Based on such distribution of local deformation, the resonators A1 and A4 act in a way similar to the first resonator eigenmode at eigenfrequency 125 Hz, as shown in figure 3(c), while resonators A2 and A3 perform in another way. Likewise, distinct modal responses are evident for resonators C1, C2, C3, and C4 at the fifth panel resonant mode around 247 Hz shown in figure 5(f). The resonators C1, C2, C3, and C4 are the resonator C specimens at the

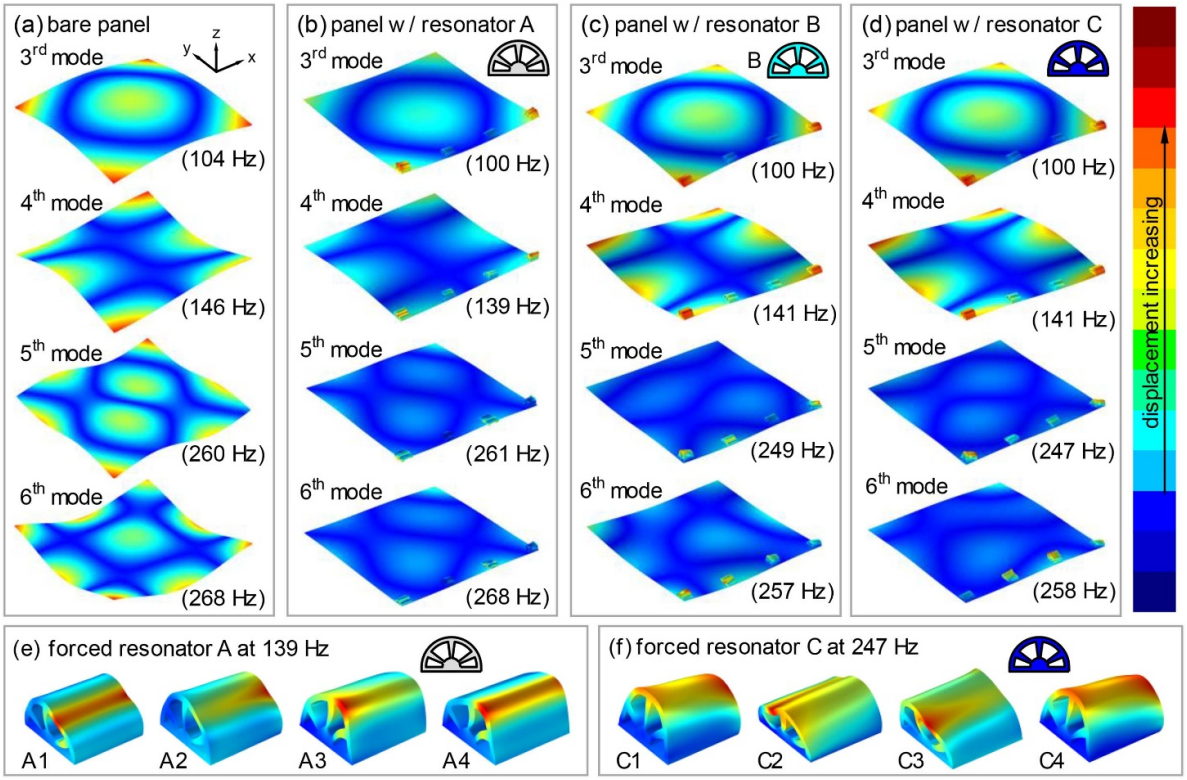

Figure 5. FE total displacement contours of (a) bare panel, panel with four (b) resonators A, (c) resonators B, (d) resonators C for the third, fourth, fifth, and sixth modes, (e) resonators A1, A2, A3, and A4 at 139 Hz, and (f) resonators C1, C2, C3, and C4 at 247 Hz under impact excitations.

positions 1, 2, 3, and 4 on the panel. The resonators C1 and C4 rock back and forth along the x- axis, which is comparable to the second eigenmode of resonator A, as shown in figure 3(c). By contrast, the displacement distributions of resonators C2 and C3 in figure 5(f) may be a combination of multiple eigenmodes.

To quantify the resonator eigenmodes that may more strongly induce panel vibration attenuation, the simulation results are evaluated for the resonators A1, A2, A3, and A4 to compute the respective ROPs under the forced panel excitation conditions. The ROPs of the forced resonators employ relative displacement components between the panel and resonator. The relative displacement components are obtained by subtracting the average displacement components of the panel surface immediately below each resonator from the resonator displacement components in the x-, y-, and z-directions. The ratio of polarization ROP_p in the p direction for the volume V of a forced resonator is

$$ROP_p = \frac{\int_V \left(u_p^f - u_p^h\right)^2 dV}{\int_V \left[\left(u_x^f - u_x^h\right)^2 + \left(u_y^f - u_y^h\right)^2 + \left(u_z^f - u_z^h\right)^2\right] dV} \tag{2}$$

Here, u_x^f, u_y^f, and u_z^f are respectively the displacement components in the x-, y-, and z-directions of the forced resonator. The u_x^h, u_y^h, and u_z^h are the average displacement components in the x-, y-, and z-directions of the host panel surface immediately below each resonator attachment location. The subscript p is respectively replaced by x, y, and z to compute the ratios of polarization in the corresponding directions.

The average ROP values of forced resonators A at frequencies around the panel forced resonant frequencies from 100 Hz to 500 Hz are presented in figure 6(a). In figures 3(a) and (b), the experimental and simulation results reveal more dramatic panel vibration attenuation in the frequency range from 250 Hz to 300 Hz. At this frequency range, figure 6(a) shows that the ROP_z values for resonators A at 261 Hz and 268 Hz vary between 74% and 75%. These results establish a first observation that resonators exhibiting greater ROP_z values lead to increased vibration attenuation. The total displacement contours of the forced resonators A1, A2, A3, and A4 at 261 Hz having greater ROP_z values are presented in figure 6(b). The four resonators A exhibit a total displacement response at 261 Hz in figure 6(b) that is similar to the fifth eigenmode of resonator A at 214 Hz, as shown in figure 3(c). Here, the eigenmode at 214 Hz is termed the *referenced* eigenmode for the resonator A, and the corresponding ROP values are presented in the far-right bar sub-plot in italic types in figure 6(a). There is only a total deviation of ROP values of 7% R between the referenced eigenmode and forced resonator responses at 261 Hz and 268 Hz, which are highlighted by darker shades in figure 6(a) along with the referenced eigenmode. These results suggest that the relative proximity between the 214 Hz referenced eigenmode for resonator A at the forced panel resonance at 261 Hz and 268 Hz results in significant activation of

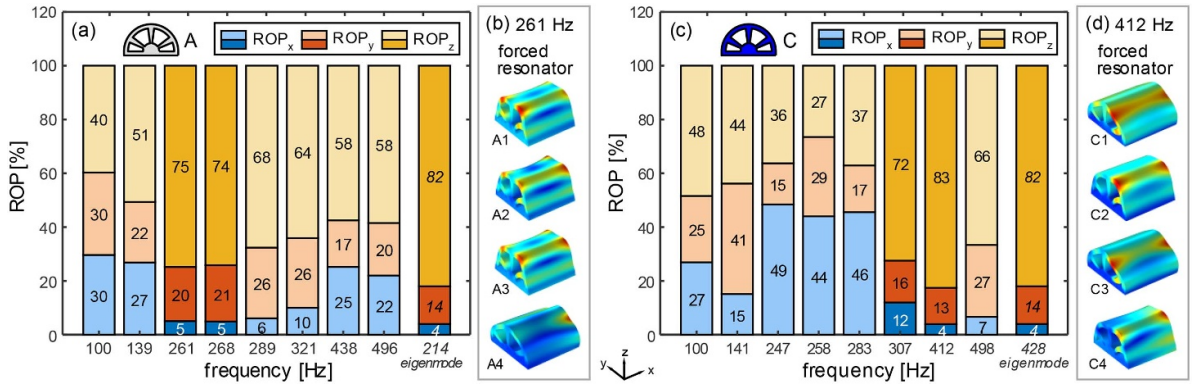

Figure 6. (a) ROP values for forced resonators A and the referenced eigenmode at 214 Hz. (b) Total displacement contours of forced resonators A at 261 Hz. (c) ROP values of forced resonators C and the referenced eigenmode at 428 Hz. (d) Total displacement contours of forced resonators C at 412 Hz. Note that the total displacement contours of referenced eigenmodes of resonators A and C are shown in the fifth eigenmode sub-plot of figure 3(c).

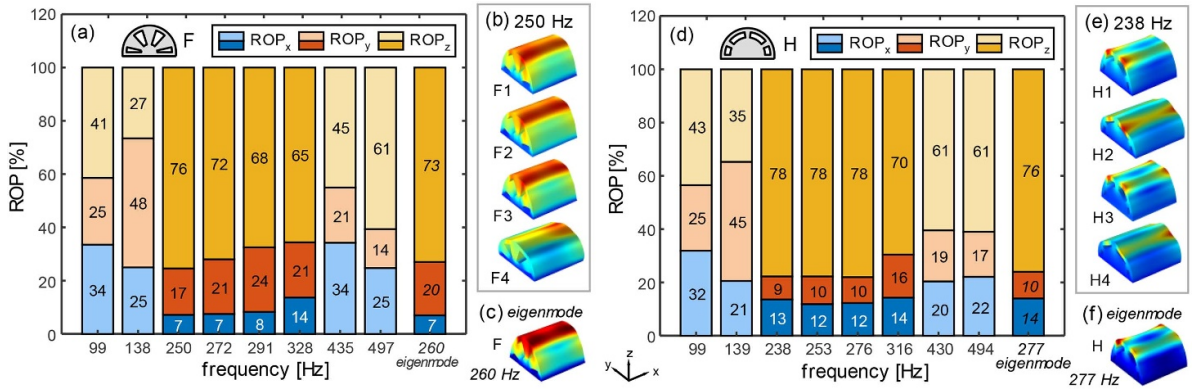

Figure 7. (a) ROPs of forced resonators F and the referenced eigenmode at 260 Hz. Total displacement contours of (b) forced resonators F at 250 Hz and (c) referenced eigenmode at 260 Hz. (d) ROPs of forced resonators H and the referenced eigenmode at 277 Hz. Total displacement contours of (e) forced resonators H at 238 Hz and (f) referenced eigenmode at 277 Hz.

the referenced eigenmode and greater vibration energy transfer to the resonators. Such trends are therefore borne out by greater ROP_z values in the forced excitation case observed in figure 6(a).

This method of analysis is applied to the forced vibration of the panels with resonators C. The resonators C are fabricated using a higher modulus material than than resonators A, see section 3.1. The ROP values for forced resonators C are respectively presented in figure 6(c). The panel with resonators C has more significant vibration attenuation in the frequency range from 300 Hz to 450 Hz in the experimental and simulation results in figures 3(a) and (b). The resonators C exhibit large ROP_z values at the forced resonances 307 Hz and 412 Hz in figure 6(c), vary between 72% and 83%. Studying the forced total displacements in figure 6(d) at 412 Hz shows that the resonators C1, C2, C3, and C4 oscillate in ways qualitatively similar to the fifth eigenmodes in figure 3(c).

The Young's modulus of resonator C is respectively four times the modulus for resonator A, while resonators A and C share the same cross-section geometry. In other words, since the eigenfrequencies of the resonator scale by a factor of the square root of the Young's modulus, the fifth eigenmode of resonators C is 428 Hz. Hence, the referenced eigenmode for resonator C is 428 Hz, which exhibits similar ROP distributions as the referenced eigenmode for resonator A, seen comparing the right-most results of each figures 6(a) and (c).

For resonators C in figure 6(c), the forced responses that lead to 10% or less ROP deviation with the referenced eigenmode are highlighted by darker shades. The displacement contours and ROP distributions in figure 6(c) reveal that the forced resonators C at 307 Hz and 412 Hz may primarily consist of modal contributions from the referenced eigenmode. These results moreover confirm that significant vibration attenuation is achieved by activating eigenmodes with greater ROP_z values.

To assess the extensibility of these findings to resonators having change in cross-section geometry parameters, the ROP values for resonators F and H are respectively presented in figures 7(a) and (d) under the forced panel vibration condition. The resonator F has a smaller open angle ratio than resonator A, which indicates that the radially arrayed beams are thicker for F compared to A. On the other hand, the resonator H has a larger radius ratio than resonator A, which indicates that the semicircular core is larger for H than for A. In figures 4(a), (b), (d) and (e), the panels with either resonators F and H exhibit

more dramatic vibration attenuation in the frequency range from 250 Hz to 350 Hz.

The ROP value distributions in figures 7(a) and (d) confirm that resonators F and resonators H have greater ROP_z values in the frequency range from 238 Hz to 328 Hz, varying from 65% to 78%. The ROP distributions for resonators F at 250 Hz and 272 Hz are especially similar to the ROP distributions for the referenced eigenmode at 260 Hz in figure 7(a). Similarly, the 277 Hz referenced eigenmode in figure 7(d) appears as a template for the ROP distributions of the forced responses of resonators H at 238 Hz, 253 Hz, and 276 Hz. The total displacement profiles of the forced resonators F at 250 Hz in figure 7(b) qualitatively emulate the total displacement of the referenced eigenmode at 260 Hz shown in figure 7(c), with similar trends borne out between resonators H and the referenced eigenmode in figures 7(e) and (f). Overall, these results further substantiate the finding that vibration energy transfer from the panel to the resonators is enhanced by way of frequency and ROP value similarity between eigenmodes and forced responses features large ROP_z values.

Based on the findings in this study, the effectiveness of the structurally-integrated resonators to mitigate panel vibration is governed by spectral and spatial similarity of forced response behavior of resonators bearing similarity to eigenmodes with large ROP_z values.

4. Conclusions

This research investigates lightweight elastomeric half cylindrical resonators as a means to suppress forced vibration of an aluminum panel while minimizing mass and coverage application from the resonator attachments. Finite element modeling and experimental undertakings help to create complementary tools to reveal vibration attenuation mechanisms manifest in the resonator and panel interaction. The influences of the cross-sectional geometry and Young's modulus on resonator dynamic behavior and vibration attenuation mechanisms are uncovered showing distinct coupling between the panel and resonators through such resonator design parameter changes. The first order eigenfrequencies of the half cylindrical resonators are seen to exert great influence on the starting mode for greater vibration attenuation, which may be tuned by the Young's modulus of the resonators. In general, it is observed that the dynamic stiffness of the resonators is more influential to tune the resonators vibration characteristics. A method for analyzing modal compositions for forced resonator dynamic response is established using a 3D finite element modeling. The analysis reveals that the eigenmode having a large percentage of polarized displacement in the z-axis may be more influential on the transverse vibration suppression. By transferring the flexural vibration from the panel to resonators, the displacement in the resonators may increase, and the panel flexural vibration may attenuate globally. These investigations may guide attention to new concepts for lightweight resonators with a small coverage area for vibration suppression in a wide variety of engineering applications.

Acknowledgments

This work is supported by The Ohio State University Simulation Innovation and Modeling Center via Honda R&D Americas, Inc.

ORCID iD

Ryan L Harne https://orcid.org/0000-0003-3124-9258

References

[1] Zheng H, Pau G S H and Wang Y Y 2006 A comparative study on optimization of constrained layer damping treatment for structural vibration control *Thin-Walled Struct.* **44** 886–96
[2] Chen Y C and Huang S C 2002 An optimal placement of CLD treatment for vibration suppression of plates *Int. J. Mech. Sci.* **44** 1801–21
[3] Chen L H and Huang S C 1999 Vibrations of a cylindrical shell with partially constrained layer damping (CLD) treatment *Int. J. Mech. Sci.* **41** 1485–98
[4] Khalfi B and Ross A 2016 Transient and harmonic response of a sandwich with partial constrained layer damping: A parametric study *Composites* B **91** 44–55
[5] Zheng H, Cai C and Tan X M 2004 Optimization of partial constrained layer damping treatment for vibrational energy minimization of vibrating beams *Comput. Struct.* **82** 2493–507
[6] Zheng W, Lei Y, Li S and Huang Q 2013 Topology optimization of passive constrained layer damping with partial coverage on plate *Shock Vib.* **20** 199–211
[7] Jin G, Yang C, Liu Z, Gao S and Zhang C 2015 A unified method for the vibration and damping analysis of constrained layer damping cylindrical shells with arbitrary boundary conditions *Compos. Struct.* **130** 124–42
[8] Oudich M, Senesi M, Assouar M B, Ruzenne M, Sun J H, Vincent B, Hou Z and Wu T T 2011 Experimental evidence of locally resonant sonic band gap in two-dimensional phononic stubbed plates *Phys. Rev.* B **84** 165136
[9] Hsu J C and Wu T T 2007 Lamb waves in binary locally resonant phononic plates with two-dimensional lattices *Appl. Phys. Lett.* **90** 201904
[10] Zhang S, Wu J H and Hu Z 2013 Low-frequency locally resonant band-gaps in phononic crystal plates with periodic spiral resonators *J. Appl. Phys.* **113** 163511
[11] Assouar M B, Sun J H, Lin F S and Hsu J C 2014 Hybrid phononic crystal plates for lowering and widening acoustic band gaps *Ultrasonics* **54** 2159–64
[12] Li Y, Zhu L and Chen T 2017 Plate-type elastic metamaterials for low-frequency broadband elastic wave attenuation *Ultrasonics* **73** 34–42
[13] Beli D, Arruda J R F and Ruzzene M 2018 Wave propagation in elastic metamaterial beams and plates with interconnected resonators *Int. J. Solids Struct.* **139** 105–20
[14] Yu D, Liu Y, Wang G, Zhao H and Qiu J 2006 Flexural vibration band gaps in Timoshenko beams with locally resonant structures *J. Appl. Phys.* **100** 124901
[15] Sugino C, Xia Y, Leadenham S, Ruzzene M and Erturk A 2017 A general theory for bandgap estimation in locally resonant metastructures *J. Sound Vib.* **406** 104–23
[16] Jensen J S 2003 Phononic band gaps and vibrations in one- and two-dimensional mass–spring structures *J. Sound Vib.* **266** 1053–78
[17] Zhu R, Liu X N, Hu G K, Sun C T and Huang G L 2014 A chiral elastic metamateiral beam for broadband vibration suppression *J. Sound Vib.* **333** 2759–73

[18] Gao P, Climente A, Sánchez-Dehesa J and Wu L 2019 Single-phase metamaterial plates for broadband vibration suppression at low frequencies *J. Sound Vib.* **444** 108–26
[19] Wang Z, Zhang Q, Zhang K and Hu G 2016 Tunable digital metamaterial for broadband vibration isolation at low frequency *Adv. Mater.* **28** 9857–61
[20] Igusa T and Xu K 1994 Vibration control using multiple tuned mass dampers *J. Sound Vib.* **175** 491–503
[21] Joshi A S and Jangid R S 1997 Optimum parameters of multiple tuned mass dampers for base-excited damped systems *J. Sound Vib.* **202** 657–67
[22] Zuo L and Nayfeh S A 2006 The two-degree-of-freedom tuned-mass damper for suppression of single-mode vibration under random and harmonic excitation *J. Vib. Acoust.* **128** 56–65
[23] Zuo L 2009 Effective and robust vibration control using series multiple tuned-mass dampers *J. Vib. Acoust.* **131** 031003
[24] Li H N and Ni X L 2007 Optimization of non-uniformly distributed multiple tuned mass damper *J. Sound Vib.* **308** 80–97
[25] Zuo L and Nayfeh S A 2004 Minimax optimization of multi-degree-of-freedom tuned-mass dampers *J. Sound Vib.* **272** 893–908
[26] Jacquot R G 2001 Suppression of random vibration in plates using vibration absorbers *J. Sound Vib.* **248** 585–96
[27] Yu T and Lesieutre G A 2017 Damping of sandwich panels via three-dimensional manufactured multimode metamaterial core *AIAA J.* **55** 1440–9
[28] Nouh M, Aldraihem O and Baz A 2015 Wave propagation in metamaterial plates with periodic local resonances *J. Sound Vib.* **341** 53–73
[29] Sun L 2017 Experimental investigation of vibration damper composed of acoustic metamaterials *Appl. Acoust.* **119** 101–7
[30] Yeh S L and Harne R L 2019 Tailoring concurrent shear and translational vibration control mechanisms in elastomeric metamaterials for cylindrical structures *Mech. Syst. Signal Process* **117** 609–33
[31] Yeh S L and Harne R L 2019 Origins of broadband vibration attenuation empowered by optimized viscoelastic metamaterial inclusions *J. Sound Vib.* **458** 218–37
[32] Avitabile P 2001 Experimental modal analysis *Sound Vib.* **35** 20–31
[33] Rao S S 2007 *Vibration of Continuous Systems* (Hoboken: Wiley)
[34] Harne R L, Song Y and Dai Q 2017 Trapping and attenuating broadband vibroacoustic energy with hyperdamping metamaterials *Extreme Mech. Lett.* **12** 41–47
[35] Chiou M J, Lin Y C, Ono T, Esashi M, Yeh S L and Wu T T 2014 Focusing and waveguiding of Lamb waves in micro-fabricated piezoelectric phononic plates *Ultrasonics* **54** 1984–90
[36] Yeh S L, Lin Y C, Tsai Y C, Ono T and Wu T T 2016 Level repulsion of GHz phononic surface waves in quartz substrate with finite-depth holes *Ultrasonics* **71** 106–10